https://doi.org/10.5194/egusphere-2026-1771
Preprint. Discussion started: 20 April 2026


# Altitude-Dependent Role of Nitric Acid in Iodic Acid-Iodous Acid Nucleation: From Marine Boundary Layer Catalyst to Upper Troposphere Core Component

Jiaze Zhang[1], Ling Liu[1], An Ning[1], Haotian Zu[1], Jing Li[1], Fengyang Bai[1,2], Jie Yang[1], and Xiuhui Zhang[1]

[1] State Key Laboratory of Environment Characteristics and Effects for Near-space, Key Laboratory of Cluster Science, Ministry of Education of China, School of Chemistry and Chemical Engineering, Beijing Institute of Technology, Beijing, 100081, China.
[2] Institute of Catalysis for Energy and Environment, College of Chemistry and Chemical Engineering, Shenyang Normal University, Shenyang, 110034, China.

*Correspondence to*: Ling Liu (lingliu@bit.edu.cn), and Xiuhui Zhang (zhangxiuhui@bit.edu.cn)

**Abstract.** With global sulfur emissions declining and concurrent marine iodine emissions rising, new particle formation (NPF) driven by iodic acid ($HIO_3$) and iodous acid ($HIO_2$) has become critical to global aerosol and cloud condensation nuclei (CCN) budget. However, the role of ubiquitous nitric acid ($HNO_3$) in this iodine-driven nucleation across altitudes from the marine boundary layer (MBL) to the upper troposphere (UT) remains poorly understood. Herein, we integrated quantum chemical calculations with Atmospheric Cluster Dynamics Code (ACDC) simulations to unravel the altitude-dependent enhancement mechanism by which $HNO_3$ enhances $HIO_3$-$HIO_2$ nucleation. Under MBL conditions, $HNO_3$ acts as a catalyst to promote nucleation via collision and re-evaporation processes, yielding a modest 2-3-fold enhancement in nucleation. In contrast, as altitude increases to the UT, where cluster evaporation is effectively suppressed by low temperature, $HNO_3$ becomes a core component of nucleation clusters, driving a 200-fold enhancement in nucleation. Consequently, the cluster formation rates of the $HNO_3$–$HIO_3$–$HIO_2$ mechanism reach $10^3$–$10^4$ $cm^{-3}$ $s^{-1}$, exceeding those of the well-documented $H_2SO_4$–$NH_3$–$HNO_3$ mechanism under comparable UT conditions. Our findings establish $HNO_3$ as a critical atmospheric agent that amplifies iodine oxoacid nucleation across altitudes, providing a critical chemical explanation for intense NPF events in both polluted coastal regions and the UT. This altitude-dependent role of $HNO_3$ links marine iodine emissions to troposphere-wide particle formation, with important implications for global CCN budgets and the refinement of climate models.

## 1 Introduction

Atmospheric aerosols exert critical impacts on air quality, human health, and global climate change (Haywood and Boucher, 2000; Pope and Dockery, 2006; Fan et al., 2016; Hirshorn et al., 2022), primarily by acting as cloud condensation nuclei (CCN) that modulate cloud microphysics (Fan et al., 2016; Li et al., 2022). New particle formation (NPF) accounts for ~ 50% of global CCN (Kulmala et al., 2013; Williamson et al., 2019) and is the dominant particle source in the upper troposphere (UT) (Gordon et al., 2017), thus serving as a key process linking atmospheric chemistry to climate regulation. Nucleation is

https://doi.org/10.5194/egusphere-2026-1771
Preprint. Discussion started: 20 April 2026


recognized as the key step in NPF processes (Zhang, 2010; Kulmala et al., 2013). Due to the chemical complexity of nucleation precursors and the sensitivities to ambient conditions, identifying molecular-level mechanisms during the critical nucleation stage remains a persistent challenge in atmospheric chemistry (Zhang et al., 2012).

Conventional sulfuric acid ($H_2SO_4$)-dominated nucleation mechanisms fail to account for the observed concentrations of particulate matter in the boundary layer and cloud condensation nuclei in the upper troposphere (Williamson et al., 2019). With declining global sulfur emissions (Aas et al., 2019) and rising marine iodine emissions (Cuevas et al., 2018; Legrand et al., 2018), recent studies have identified marine-derived iodine oxoacids, iodic acid ($HIO_3$) (Sipilä et al., 2016) and iodous acid ($HIO_2$) (He et al., 2021), as important nucleation precursors in marine (Liu et al., 2023; Bai et al., 2025), polar (Baccarini et al., 2020; He et al., 2021; Li et al., 2024a), and even high-altitude environments (Koenig et al., 2020; Salignat et al., 2024; Li et al., 2024b). Studies show that $HIO_3$ and $HIO_2$ can form stable clusters via acid–base interactions and halogen bonds (Liu et al., 2023; Ma et al., 2023). However, this binary $HIO_3$–$HIO_2$ nucleation mechanism alone cannot explain the intense NPF events observed in polluted coastal regions (e.g., Zhejiang, China), suggesting that additional atmospheric species may participate in and promote iodine oxoacid-driven nucleation processes (Yu et al., 2019; Ma et al., 2023), yet these species remain unidentified and uncharacterized.

Nitric acid ($HNO_3$) is one of the most widespread and abundant inorganic acids in the atmosphere, present throughout the marine boundary layer (MBL) and upper troposphere (UT), with sources including anthropogenic emissions (Wang et al., 2021) and natural processes such as lightning (Tost, 2017). Previous studies have confirmed that $HNO_3$ stabilizes atmospheric molecular clusters via hydrogen bonds and proton transfer-driven electrostatic interactions in both $H_2SO_4$–dimethylamine (DMA) (Liu et al., 2021) and $H_2SO_4$–$NH_3$ (Liu et al., 2018; Wang et al., 2022) nucleation systems. Importantly, $HNO_3$ and iodine precursors extensively coexist across altitudes. Specifically, nitrate and iodate are simultaneously detected in the free troposphere (FT) (Frege et al., 2017), and both iodine species (Koenig et al., 2020) and $HNO_3$ are observed in the UT (Jurkat et al., 2014). However, nitrate-based chemical ionization, commonly used for neutral cluster detection, tends to mask $HNO_3$'s involvement in iodine-driven nucleation (Sipilä et al., 2016), leaving its molecular mechanism and environmental dependence unclear.

Notably, atmospheric temperature, condensation sink, and precursor concentrations vary sharply with altitude, giving rise to strong altitude-dependent behavior in atmospheric nucleation. To date, no study has revealed how $HNO_3$ regulates iodine oxoacid nucleation from the MBL to the UT. Consequently, fundamental questions remain unanswered: Can $HNO_3$ interact with $HIO_3$ and $HIO_2$ to form critical nucleation clusters? What is the molecular mechanism by which $HNO_3$ interacts with $HIO_3$–$HIO_2$ clusters? How does the role of $HNO_3$ in $HIO_3$–$HIO_2$ nucleation shift with altitude from the MBL to the UT? Answering these questions will help us elucidate how marine iodine emissions shape troposphere-wide NPF and the global CCN budget under the sulfur emission reduction.

Here, we combine high-level quantum chemical calculations and Atmospheric Cluster Dynamics Code (ACDC) (McGrath et al., 2012) simulations to systematically unravel the altitude-dependent mechanism of the role of $HNO_3$ in $HIO_3$–$HIO_2$ nucleation. We reveal the molecular nature of iodine-containing cluster stabilization by $HNO_3$, quantify nucleation rates

https://doi.org/10.5194/egusphere-2026-1771
Preprint. Discussion started: 20 April 2026


and pathway evolution along the vertical atmospheric profile, and evaluate the new mechanism against classic nucleation schemes. Our results establish the functional transition of $HNO_3$ from a catalyst in the MBL to a core cluster component in the UT, providing critical theoretical support for interpreting global iodine-driven NPF and improving aerosol representations in climate models.

## 2 Methods

### 2.1 Quantum Chemistry Calculation

This study employed a systematic, multi-step computational strategy to explore the structural configurations and thermodynamic properties of $(HNO_3)_x(HIO_3)_y(HIO_2)_z$ clusters ($2 \le x + y + z \le 6$, $1 \le x \le 3$), with detailed procedures provided in the Supporting Information. The initial structures of $(HIO_3)_y(HIO_2)_z$ ($2 \le y + z \le 6$) clusters were adopted from our previous study (Liu et al., 2023; Zu et al., 2024). All identified low-energy cluster conformations were rigorously optimized and subjected to frequency analysis using the Gaussian 09 package (Frisch et al., 2009) at the $\omega$B97X-D/6-311++G(3df,3pd) (for H, O, N) + aug-cc-pVTZ-PP with ECP28MDF (for I) level of theory (Francl et al., 1982; Peterson et al., 2003), employing FineGrid and tight convergence.

The Gibbs free energies ($\Delta G$, kcal $mol^{-1}$) of the optimized clusters at a reference pressure of 1 atm were calculated using the following equation:

$$\Delta G = \Delta E_{\text{DLPNO-CCSD(T)}} + \Delta E_{\text{SOC}} + \Delta G_{\text{thermal}}^{\omega\text{B97X-D}} \quad (1)$$

The terms in eq 1 were derived as follows: (1) The electronic energy term ($\Delta E_{\text{DLPNO-CCSD(T)}}$), intended to refine binding energies with high accuracy, was obtained from the single point calculations using ORCA 5.0 program (Neese, 2012) at the DLPNO-CCSD(T)/aug-cc-pVTZ (for H, O, and N) + aug-cc-pVTZ-PP with ECP28MDF (for I) level of theory with TightPNO and TightSCF settings. (2) The spin–orbit coupling (SOC) effects ($\Delta E_{\text{SOC}}$), specific to iodine-containing clusters, were evaluated via the Gaussian 16 package (Frisch et al., 2016) at the $\omega$B97X-D/6-311++G(3df,3pd) (for H, O and N) + dhfTZVP-2c (for I) level to capture accurate electronic properties of the heavy element iodine (Chan and Yim, 2013; Kühn and Weigend, 2015; Sarr et al., 2021; Holzer et al., 2022). (3) Temperature-dependent free energy corrections ($\Delta G_{\text{thermal}}^{\omega\text{B97X-D}}$) were computed at the $\omega$B97X-D/6-311+ +G(3df,3pd) (for H, O, and N) + aug-cc-pVTZ-PP with ECP28MDF (for I) level. The Shermo 2.6 code (Lu and Chen, 2021) was used to calculate free energy values at specified atmospheric temperatures (204-288 K).

### 2.2 Wave Function Analysis

The wavefunction from quantum calculations was analyzed using Multiwfn 3.7 (Lu and Chen, 2012) with results visualized via VMD software (Humphrey et al., 1996), to investigate the intermolecular interactions responsible for the identified cluster conformations. Potential binding sites were identified by mapping the electrostatic potential (ESP) onto the Van der Waals (vdW) surface, defined by the 0.001 a.u. electron density contour, to distinguish electron-rich (electronegative) and electron-

https://doi.org/10.5194/egusphere-2026-1771
Preprint. Discussion started: 20 April 2026


deficient (electropositive) regions prone to noncovalent bonding. For quantitative evaluation of interaction strengths, the Atoms in Molecules (AIM) theory (Lane et al., 2013) was employed to calculate key topological properties at bond critical points (BCPs), including electron density $\rho(r)$, Laplacian of electron density $\nabla^2\rho(r)$, and local energy density $H(r)$, as shown in Table S2.

### 2.3 Atmospheric cluster dynamics code (ACDC) simulation

To quantitatively investigate nucleation kinetics, including cluster formation rates and growth pathways, the ACDC (McGrath et al., 2012) was employed to numerically solve the birth-death equations (Eq. 2). These equations describe the temporal evolution of cluster concentrations by integrating collision, evaporation, source, and sink processes:

$$\frac{\mathrm{d}c_i}{\mathrm{d}t} = \frac{1}{2}\sum_{j<i}\beta_{j,(i-j)}c_j c_{(i-j)} + \sum_j \gamma_{(i+j)\to i}c_{i+j} - \sum_j \beta_{i,j}c_i c_j - \frac{1}{2}\sum_{j<i}\gamma_{i\to j}c_i + Q_i - S_i \quad (2)$$

where $c_i$ denotes the concentration of cluster $i$, $\beta_{j,(i-j)}$ represents the collision rate coefficient between clusters $j$ and $(i - j)$, and $\gamma_{(i+j)\to i}$ corresponds to the evaporation rate coefficient for cluster $(i + j)$ dissociating into clusters $i$ and $j$. External sources and size-dependent sinks are quantified by $Q_i$ and $S_i$, respectively. Details for calculating $\beta_{j,(i-j)}$ and $\gamma_{(i+j)\to i}$ are presented in the Supporting Information. In the ACDC simulations, kinetically stable clusters are characterized as those capable of continuous growth rather than dissociation via evaporation, as quantified by the criterion $\beta c/\sum\gamma > 1$. Correspondingly, the boundary condition specifies the smallest kinetically stable clusters that can grow beyond the simulation box. Boundary clusters were determined individually for each ACDC simulation: temperature-dependent $\beta$ and $\sum\gamma$ coefficients were first calculated for each cluster, and those satisfying the criterion $\beta c/\sum\gamma > 1$ at the given monomer concentration ($c$) were defined as boundary clusters.

To account for intermolecular vdW force enhancement, a factor of 2.3 was applied to $\beta_{i,j}$, consistent with prior simulations (Halonen et al., 2019). Additionally, a size-dependent sink term (Lehtipalo et al., 2016) $S_i$ is used to quantify cluster losses:

$$S_i = \mathrm{CS}_{\mathrm{ref}} \times \left(d_i / d_{\mathrm{ref}}\right)^{-m} \quad (3)$$

where $d_i$ is the diameter of cluster $i$, $\mathrm{CS}_{\mathrm{ref}}$ is the condensation sink for a reference monomer, and $m$ is set to 1.7, which depends on scavenger distributions and is consistent with typical atmospheric aerosols (Lehtinen et al., 2007).

## 3 Results and Discussion

### 3.1 Molecular Interactions

The formation of thermodynamically stable atmospheric clusters is governed by intermolecular interactions between nucleation precursors, primarily hydrogen bonds (HB) and halogen bonds (XB). To identify potential binding sites between $HNO_3$ and iodine oxoacids, we analyzed their molecular electrostatic potential (ESP, Figure 1), which maps the electron-rich (electronegative) and electron-deficient (electropositive) regions on the molecular surface, where noncovalent bonds are prone to form. The ESP analysis indicates that $HNO_3$ can interact with iodine oxoacids through diverse bonding modes, reflecting

https://doi.org/10.5194/egusphere-2026-1771
Preprint. Discussion started: 20 April 2026


its dual role as both a halogen bond acceptor and a hydrogen bond donor. For halogen bonding, the nitro oxygen atoms of $HNO_3$ exhibit a localized negative ESP (-18.7 kcal $mol^{-1}$), providing accessible sites to accept halogen bonds from the electrophilic iodine centers of $HIO_3$ and $HIO_2$. More critically, the hydroxyl hydrogen of $HNO_3$ displays a highly positive ESP (+67.9 kcal $mol^{-1}$), which is significantly more electropositive than the hydroxyl hydrogen sites in $HIO_3$ (+59.1 kcal $mol^{-1}$) or $HIO_2$ (+57.3 kcal $mol^{-1}$). This enhanced electropositivity enables $HNO_3$ to act as a superior proton donor, favoring proton transfer to the electron-rich site during cluster formation.

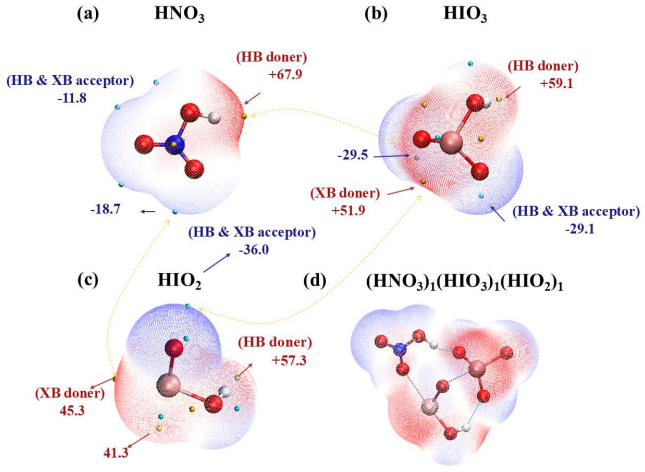


**Figure 1.** The electrostatic potential (ESP, kcal $mol^{-1}$)-mapped molecular van der Waals surfaces of (a) $HNO_3$, (b) $HIO_3$, (c) $HIO_2$, and (d) the $(HNO_3)_1(HIO_3)_1(HIO_2)_1$ cluster. Yellow and cyan dots denote the positions of ESP maxima and minima, respectively. Yellow dashed arrows highlight the key intermolecular interaction orientations within $(HNO_3)_1(HIO_3)_1(HIO_2)_1$ cluster. Blue dashed lines represent hydrogen bonds, and purple dashed lines represent halogen bonds. White, blue, red, and pink spheres represent H, N, O, and I atoms, respectively.

To confirm the dominant binding modes, we employed a multi-step conformational search strategy, we identified the most stable configurations of $(HNO_3)_x(HIO_3)_y(HIO_2)_z$ clusters ($2 \le x + y + z \le 6$, $1 \le x \le 3$) as shown in Figure S1. In these optimized clusters, $HNO_3$ molecules form thermodynamically stable structures with iodine oxoacids ($HIO_3$/$HIO_2$) via an interaction network bridged by hydrogen bonds and halogen bonds. Within this ternary system, $HNO_3$ and $HIO_3$ act as proton donors (acids), while $HIO_2$ serves as the proton acceptor (base) due to its stronger basicity relative to the acids. Both $HNO_3$ and $HIO_3$ undergo proton transfer to $HIO_2$, thereby forming ion pairs that substantially enhance cluster stability by strengthening electrostatic interactions.

To quantitatively characterize the strength of these intermolecular interactions, we performed AIM analysis (Table S2). The results confirm that $HNO_3$ acts primarily as a hydrogen bond donor rather than a halogen bond acceptor. $HNO_3$ accounts for 80% of all HBs, the majority of which are medium-strength bonds (Emamian et al., 2019) (68.3% exhibit binding energies

https://doi.org/10.5194/egusphere-2026-1771
Preprint. Discussion started: 20 April 2026


of 12.0–24.0 kcal mol$^{-1}$, with $\nabla^2\rho(r) > 0$ and $H(r) < 0$). These HBs are comparable in strength to those formed between iodine oxoacids themselves, highlighting $HNO_3$'s contribution to the hydrogen bonding network. By comparison, $HNO_3$ contributes 37% of all XBs in the ternary clusters. The N–O···I XBs formed between $HNO_3$ and iodine oxoacids are weaker (average $\rho(r)$: 0.036 a.u.; average bond length: 2.7 Å) than the XBs formed between iodine oxoacids (average $\rho(r)$: 0.054 a.u.; average bond length: 2.4 Å).

### 3.2 Cluster Stability

To elucidate the stability of the $HNO_3$-$HIO_3$-$HIO_2$ clusters, we evaluated their thermodynamic and kinetic properties (Figure 2). Thermodynamic analysis reveals a distinct acid-base stoichiometry dependence of cluster stability (Figure 2(a)). Six-molecule clusters with an acid-to-base ratio of 1:1 ($HNO_3$ and $HIO_3$ as acids, $HIO_2$ as base) exhibit the lowest Gibbs free energies of formation ($\Delta G$). This 1:1 stoichiometry preference is consistent across all cluster sizes (Figure S2). Notably, for clusters with fixed molecular count and acid-base ratio, increasing the $HNO_3$ fraction elevates $\Delta G$ across all sizes (Figure S2). This trend indicates that $HNO_3$–$HIO_2$ clusters and $HNO_3$–$HIO_3$–$HIO_2$ clusters are less thermodynamically stable than $HIO_3$–$HIO_2$ clusters, reflecting the combined effects of hydrogen bonding and halogen bonding on overall cluster stability.

While negative $\Delta G$ reflects the thermodynamic feasibility of cluster formation, the kinetic competition between collision–driven growth and evaporation–driven dissociation ultimately determines whether clusters can persist and grow into larger clusters. To assess kinetic feasibility, we calculated the minimum $HNO_3$ concentration required for clusters to achieve kinetic stability ($\beta c_{boundary}/\Sigma\gamma = 1$, where collision rate equals evaporation rate) across tropospheric temperatures (228–288 K, Figure 2(b)) (Dunne et al., 2016; Williamson et al., 2019). Above $c_{boundary}$, cluster growth dominates over dissociation, enabling persistent nucleation.

Although $HNO_3$-containing clusters require a higher $c_{boundary}$ than $HIO_3$–$HIO_2$ clusters, ambient $HNO_3$ concentrations ($10^8$–$10^{11}$ molecules/cm$^3$), spanning clean polar regions to polluted coastal environments, universally exceed the $c_{boundary}$ across all tropospheric temperatures. This confirms that $HNO_3$-containing clusters are kinetically viable for growth under real atmospheric conditions. Critical to our altitude-dependent hypothesis, $c_{boundary}$ decreases sharply with declining temperature (Figure 2(b)). For the $(HNO_3)_1(HIO_3)_2(HIO_2)_3$ cluster, $c_{boundary}$ drops from ~$10^9$ molecules cm$^{-3}$ at 288 K (MBL) to ~$10^5$ molecules cm$^{-3}$ at 228 K (UT). This four-order-of-magnitude reduction demonstrates that high-altitude low temperatures drastically suppress cluster evaporation, allowing $HNO_3$ to more effectively stabilize clusters by lowering the concentration threshold for kinetic stability.

https://doi.org/10.5194/egusphere-2026-1771
Preprint. Discussion started: 20 April 2026


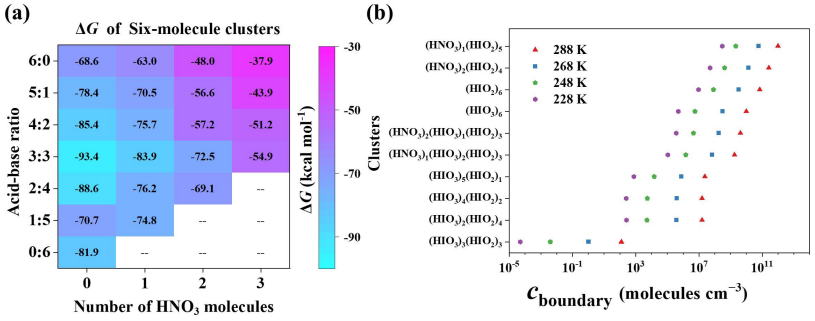


**Figure 2.** (a) Gibbs free energies of formation ($\Delta G$, kcal mol$^{-1}$) for the most stable six-molecule $HNO_3$–$HIO_3$–$HIO_2$ clusters at the DLPNO-CCSD(T)/aug-cc-pVTZ(-PP)//$\omega$B97X-D/6-311++G(3df,3pd) + aug-cc-pVTZ-PP level of theory (288 K). (b) Minimum $HNO_3$ concentrations ($c_{boundary}$) required for six-molecule clusters to reach kinetic stability at various tropospheric temperatures, defined by the condition where the collision frequency equals the total evaporation coefficients ($\beta c_{boundary} = \Sigma\gamma$). Clusters are sorted in ascending order of $c_{boundary}$. Figure S3 presents data for clusters with higher $HNO_3$ $c_{boundary}$ values and collisions involving other monomers ($HIO_3$ and $HIO_2$).

### 3.3 Cluster Formation Rates under Different Atmospheric conditions

The widespread coexistence of $HNO_3$ and iodine oxoacids ($HIO_3$/$HIO_2$) across diverse atmospheric environments, from polluted coastal MBL to remote UT, motivates a systematic investigation of the cluster formation rate ($J$) of the $HNO_3$–$HIO_3$–$HIO_2$ ternary system under altitude-resolved tropospheric conditions (Figure 3), focusing on how $HIO_3$'s contribution to $J$ evolves with altitude. We selected four temperatures strictly matching tropospheric vertical gradients: 288 K (MBL), 268 K (polar boundary layer), 248 K (FT), and 228 K (UT) (Dunne et al., 2016). The condensation sink (CS), which quantifies cluster scavenging, was set to $1\times10^{-2}$ s$^{-1}$ (polluted MBL, high background aerosols) and $1\times10^{-4}$ s$^{-1}$ (clean UT, low background aerosols) (Ranjithkumar et al., 2021), directly reflecting observed CS vertical trends. $HNO_3$ concentrations were set to $10^8$ – $10^{11}$ molecules cm$^{-3}$ (from remote polar regions to polluted coastal areas (Honrath et al., 2002; Jurkat et al., 2014; Xu et al., 2018)), and $HIO_3$ concentrations ranged between $10^5$ and $10^8$ molecules cm$^{-3}$ (from inland to coastal environments), directly mirroring their observed environmental gradients (Sipilä et al., 2016; He et al., 2021; Ning et al., 2024). Given that $HIO_2$ and $HIO_3$ are homologous iodine species with co-varying concentrations, [$HIO_2$] was defined as a fraction of [$HIO_3$]. Reported [$HIO_3$]/[$HIO_2$] ratios range from ~20 to 100 (Sipilä et al., 2016; Baccarini et al., 2020; He et al., 2023), and we adopted a ratio of 50, consistent with field observations at Mace Head (Sipilä et al., 2016) and our previous studies (Li et al., 2024c; Zu et al., 2023, 2024).

High-altitude environments drastically boost the ternary nucleation efficiency via the synergistic decline of temperature and CS with altitude. Thermodynamically, lower temperatures suppress cluster evaporation. At a constant CS ([$HNO_3$] = $10^{10}$ molecules cm$^{-3}$, and [$HIO_3$] = $10^7$ molecules cm$^{-3}$), the temperature decline from MBL (288 K) to UT (228 K) enhances $J$ by more than four orders of magnitude (from ~ $10^1$ to ~$10^5$ cm$^{-3}$ s$^{-1}$). Kinetically, the CS reduction from $1\times10^{-2}$ s$^{-1}$ (polluted lower

https://doi.org/10.5194/egusphere-2026-1771
Preprint. Discussion started: 20 April 2026


atmosphere) to $1\times10^{-4}$ $s^{-1}$ (clean UT) minimizes scavenging of nascent clusters This enhancement is especially important at low iodine oxoacid and $HNO_3$ concentrations, where clusters form slowly and are therefore more easily scavenged.

Moreover, *J* exhibits a strong dependence on the concentrations of $HNO_3$ and iodine oxoacids. As expected, higher precursor concentrations lead to higher *J*. Notably, the system's sensitivity to nucleation precursor concentrations is strongly altitude-dependent, as visualized by *J* contour orientations (Figure 3). In the MBL (e.g., 288 K), contours are nearly vertical, which indicates iodine oxoacids dominate nucleation, and $HNO_3$ only effectively enhances *J* at high $HNO_3$ concentrations (> $10^{10}$ molecules $cm^{-3}$). In contrast, as temperature decreases with increasing altitude, the contours gradually pivot towards the $[HNO_3]$ axis. At typical UT temperatures (e.g., 228 K), the contour slope approaches -1 across all simulated CS values, demonstrating that $HNO_3$ exerts a pronounced influence over a broader concentration range than at lower altitudes. Consistent with this, $HNO_3$'s enhancement factor rises to ~$10^2$ in the UT (Figure S4), confirming its transition to a critical contributor to nucleation. Given the ppb-level $HNO_3$ concentrations observed in the UT, this enhanced sensitivity underscores the amplified importance of $HNO_3$ in iodine oxoacid nucleation at high altitudes.

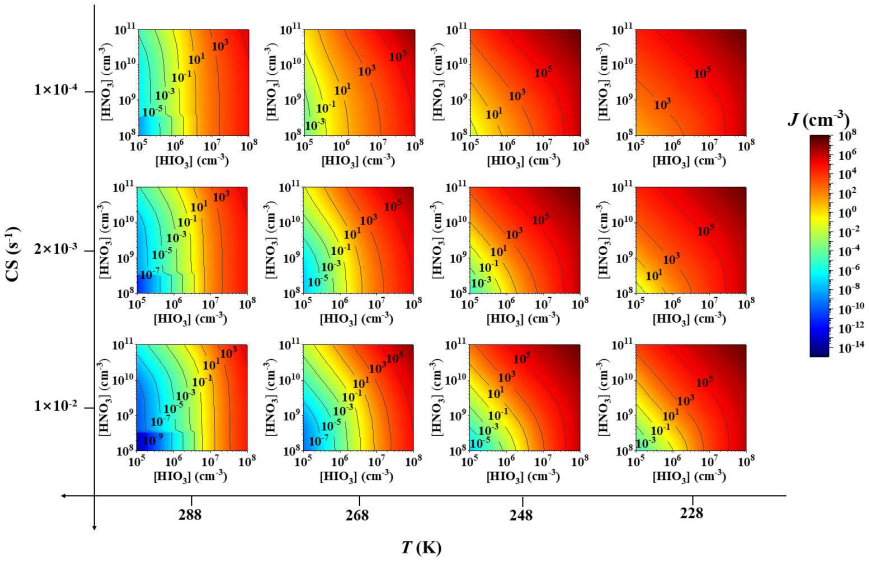


**Figure 3.** Heatmaps of (a) cluster formation rates (*J*, in $cm^{-3}$ $s^{-1}$) as a function of $HNO_3$ and $HIO_3$ concentrations, simulated under various temperature (*T*) and CS conditions. The $HIO_2$ concentration was set to $[HIO_3]/50$. *J* is represented by a color gradient from blue ($10^{-13}$ $cm^{-3}$ $s^{-1}$) to red ($10^{7}$ $cm^{-3}$ $s^{-1}$), with contour lines indicating *J* values of $10^{-9}$, $10^{-7}$, $10^{-5}$, $10^{-3}$, $10^{1}$, $10^{3}$, and $10^{5}$ $cm^{-3}$ $s^{-1}$.

High-altitude regions are critical for nucleation, as they significantly influence global CCN (Gordon et al., 2017). While $HNO_3$'s regulatory role is expected to be altitude-dependent, its quantitative variation across the troposphere remains unclear.

https://doi.org/10.5194/egusphere-2026-1771
Preprint. Discussion started: 20 April 2026


To address this gap, we quantified the $HNO_3$–$HIO_3$–$HIO_2$ nucleation mechanism by simulating the evolution of its $J$ along idealized and representative vertical atmospheric profiles. For clarity and ease of discussion, the vertical atmosphere was approximately stratified into the MBL (0–2 km), FT (2–12 km), and UT, (12–14 km), matching the concentration distributions of the nucleation precursors at different altitudes in the atmosphere (Jurkat et al., 2014).

A uniform temperature lapse rate of 6 K $km^{-1}$ (starting from 288 K at the surface) (Catling and Kasting, 2017) and a CS decline from $2\times10^{-3}$ to $1\times10^{-4}$ $s^{-1}$ (Ranjithkumar et al., 2021), were applied to reflect the transition from particle–rich MBL to clean FT. Precursor vertical concentrations were constrained as follows: the $HNO_3$ concentration was set to $1\times10^{10}$ molecules $cm^{-3}$ in the MBL (anthropogenic coastal conditions), decreasing to $1\times10^{9}$ molecules $cm^{-3}$ in the FT, and increasing to a constant $5\times10^{9}$ molecules $cm^{-3}$ (sub-ppb to ppb level) in the UT (Jurkat et al., 2014). $HIO_3$ concentration was set to $1\times10^{7}$ molecules $cm^{-3}$ in the MBL (coastal emission hotspot) (Sipilä et al., 2016) and reduced by one order of magnitude in the FT. Due to limited field constraints on $HIO_3$ at high altitudes, its concentration was held constant above the FT. This assumption is based on the fact that the concentration of iodine monoxide (IO) radical, a key precursor of $HIO_3$ in the troposphere with relatively stable concentrations across altitudes (Koenig et al., 2020; Finkenzeller et al., 2023), exhibits an observed positive correlation with that of $HIO_3$ in the troposphere. $HIO_2$ concentration was fixed at a ratio of 1/50 relative to $HIO_3$ across all altitudes, consistent with the conditions in Figure 3.

Based on the above constrained simulation conditions, we partitioned the altitude–dependent evolution of $J$ into four stages (Figure 4(e, f)). In Stage 1 (0–2 km, from the MBL to the lower FT), as altitude increases, the suppressive effects of decreasing $HNO_3$ and $HIO_3$ concentrations outweigh the promoting effects of lower temperature and reduced CS, resulting in a $J$ minimum. Near 2 km, $J$ is ~70-fold lower than that in the MBL. At this stage, the enhancement factor of $HNO_3$ ($R$, defined as $J$($HNO_3$–$HIO_3$–$HIO_2$)/$J$($HIO_3$–$HIO_2$)) is approximately 1.5–2, which indicates a modest promotional effect of $HNO_3$. In Stage 2 (2–12 km, FT), with precursor concentrations held constant, the continuous decline in temperature emerges as the dominant driver, boosting $J$ for both the binary ($HIO_3$–$HIO_2$) and ternary ($HNO_3$–$HIO_3$–$HIO_2$) mechanisms. Notably, the ternary mechanism shows a steeper altitude-dependent increase in $J$, reflecting stronger $HNO_3$ stabilization at low temperatures, with $R$ reaching $10^2$ at 8 km. Comparison of altitude–dependent trends reveals distinct "sensitive zones" where $J$ responds most sharply to altitude. For the binary $HIO_3$–$HIO_2$ mechanism, this zone is confined to a relatively narrow layer (8–10 km). By comparison, the $J$ of the ternary $HNO_3$–$HIO_3$–$HIO_2$ mechanism not only achieves a higher peak but also sustains rapid growth over a broader vertical range (2–8 km), highlighting its efficacy across a wider altitude span. In Stage 3 (12–13 km, UT), $J$ becomes less sensitive to further temperature decreases (Figure S5). At these ultra-low temperatures, thermodynamically favorable $HNO_3$-containing clusters (e.g., $HNO_3$–$HIO_2$ clusters) are effectively stabilized against evaporation (Figure S3), while elevated UT $HNO_3$ becomes the key driver of enhancement. Under these conditions, the elevated $HNO_3$ concentrations in the UT, sustained by lightning–driven chemical production and long–range transport, become the key driver of $R$ for $HIO_3$–$HIO_2$ nucleation, pushing $R$ to even higher values. In Stage 4 (13–14 km, upper UT), $J$ approaches a steady state as $HNO_3$ concentrations stabilize at ppb levels and temperature effects saturate.

https://doi.org/10.5194/egusphere-2026-1771
Preprint. Discussion started: 20 April 2026


Overall, $J$ for both $HIO_3$–$HIO_2$ and $HNO_3$–$HIO_3$–$HIO_2$ mechanisms exhibit non-monotonic altitude profiles, declining from the MBL to ~2 km then increasing toward the UT. Critically, while $HNO_3$'s enhancement on $J$ is modest at lower altitudes, its influence increases significantly with altitude, particularly in the UT where the synergy of elevated $HNO_3$ concentrations and ultra-low temperatures strongly accelerates $J$. Deep convective systems can actively transport iodine oxoacids upward into the UT (Twohy et al., 2002; Randel et al., 2010; Williamson et al., 2019), while lightning-driven oxidation sustains ppb-level $HNO_3$; conversely, UT-nucleated particles may descend via large-scale subsidence to replenish lower-tropospheric CCN (Wang et al., 2016; Xiao et al., 2023; Mehra et al., 2026). Through this bidirectional vertical coupling, $HNO_3$ acts as a bridge between marine iodine emissions at the surface and particle formation across the full tropospheric column.

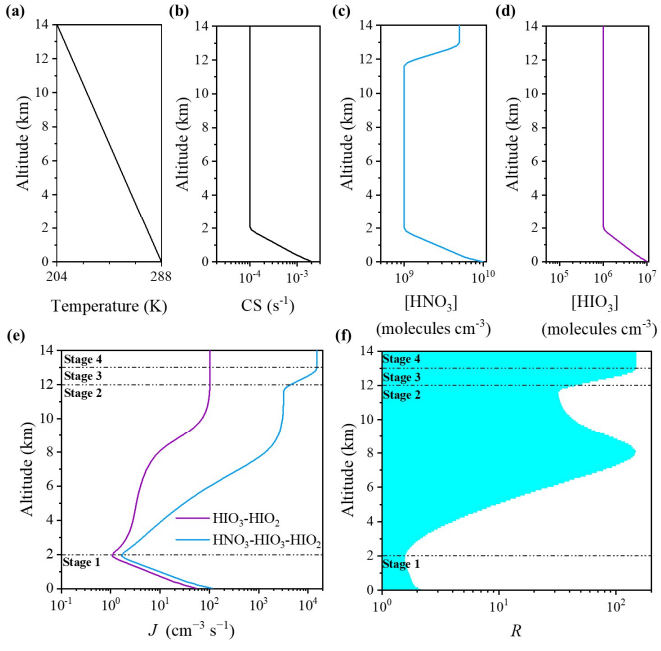


**Figure 4.** Altitude-dependent simulation inputs and the corresponding cluster formation rates ($J$, $cm^{-3}$ $s^{-1}$). (a) Temperature; (b) CS; (c) $HNO_3$ concentration; and (d) $HIO_3$ concentration as functions of altitude. (e) $J$ versus altitude for the $HIO_3$–$HIO_2$ (purple) and $HNO_3$–$HIO_3$–$HIO_2$ (blue) mechanisms, simulated under the vertical profiles in (a–d); dashed lines denote boundaries of the four altitude stages. (f) Altitude-dependent enhancement factor of $HNO_3$ ($R$, $J$($HNO_3$–$HIO_3$–$HIO_2$)/$J$($HIO_3$–$HIO_2$)) of $HIO_3$–$HIO_2$ nucleation by $HNO_3$.

### 3.4 Altitude-Dependent Nucleation Mechanisms

To uncover the molecular origin of $HNO_3$'s altitude-dependent enhancement, we analyzed the nucleation pathways of the $HNO_3$–$HIO_3$–$HIO_2$ system (Figure 5). As illustrated in Figure 5(a), ACDC simulations identify three primary nucleation routes:

https://doi.org/10.5194/egusphere-2026-1771
Preprint. Discussion started: 20 April 2026


the binary $HIO_3$–$HIO_2$ pathway, the ternary $HNO_3$–$HIO_3$–$HIO_2$ pathway, and the binary $HNO_3$–$HIO_2$ pathway. Their branching ratios evolve systematically with altitude, with $HNO_3$-involved pathways gaining dominance at higher altitude, directly reflecting $HNO_3$'s role transition (Figure 5(b)). Specifically, the binary $HIO_3$–$HIO_2$ pathway dominates at 0–6 km; above 6 km, the ternary $HNO_3$–$HIO_3$–$HIO_2$ pathway takes the lead, while the binary $HNO_3$–$HIO_2$ pathway also begins to contribute. In the UT, the high concentration of $HNO_3$ drives the binary $HNO_3$–$HIO_2$ pathway to become predominant.

$HNO_3$ promotes nucleation via both direct and indirect pathways. Directly, as a core component, $HNO_3$ is stably incorporated into growing clusters. For instance, in the binary $HNO_3$–$HIO_2$ pathway, nucleation proceeds via the stepwise addition of $(HNO_3)_1(HIO_2)_1$ dimers to form $(HNO_3)_2(HIO_2)_2$ tetramers, which subsequently collide to exceed cluster size. Additionally, $HNO_3$ participates in forming kinetically stable clusters (e.g., $(HNO_3)_1(HIO_3)_2(HIO_2)_3$, $(HNO_3)_2(HIO_3)_1(HIO_2)_3$, and $(HNO_3)_2(HIO_2)_4$). Indirectly, as a catalyst, $HNO_3$ promotes nucleation via a collision–re-evaporation cycle. Specifically, $HNO_3$ forms intermediates with $HIO_2$ (e.g., $(HNO_3)_1(HIO_2)_1$). When these intermediates collide with iodine-containing clusters, $HNO_3$ molecule re-evaporates into the gas phase while $HIO_2$ is retained, efficiently transferring $HIO_2$ to particles and accelerating nucleation.

To further elucidate $HNO_3$'s role across altitudes, Figure 5(c) presents the weighted average molecular composition of outflux clusters (weighted by pathway branching ratios), capturing its altitude-driven functional shift. In the low-to-mid troposphere (0–6 km), $HNO_3$ constitutes <10% of outflux clusters (dominated by $HIO_3$/$HIO_2$), confirming its catalytic role (collision-re-evaporation cycle), resulting in modest enhancement (< 10-fold). Above 6 km, the proportion of $HNO_3$ in outflux clusters rises steadily, exceeding 40% in the UT, signaling its transition to a core component. This shift is accompanied by a much more significant promotional effect reaching a $R$ of up to 200-fold (Figure 4(f)).

The altitude-dependent role transition of $HNO_3$ is driven by the different temperature sensitivities of evaporation (far more sensitive) versus collision coefficients (Supplementary Methods). This temperature sensitivity leads to fundamentally different nucleation behaviors: at low altitudes, rapid evaporation ensures that only the most thermodynamically stable clusters survive; at high altitudes, suppressed evaporation shifts the controlling factor to precursor availability.

At low altitudes (MBL), evaporation-limited conditions favor 1:1 acid-base stoichiometry (minimal evaporation rates, Figure 5c) in both binary $HIO_3$–$HIO_2$ and ternary $HNO_3$–$HIO_3$–$HIO_2$ pathways. With increasing altitude and decreasing temperature, evaporation is suppressed and nucleation becomes collision-limited, factoring the most abundant species. For ternary nucleation mechanism, high $HNO_3$ concentrations (exceeding iodine oxoacids) drive more frequent $HNO_3$–$HIO_2$ collisions, making $HNO_3$–involved pathways dominant in the UT (Figure 5(b)).

https://doi.org/10.5194/egusphere-2026-1771
Preprint. Discussion started: 20 April 2026


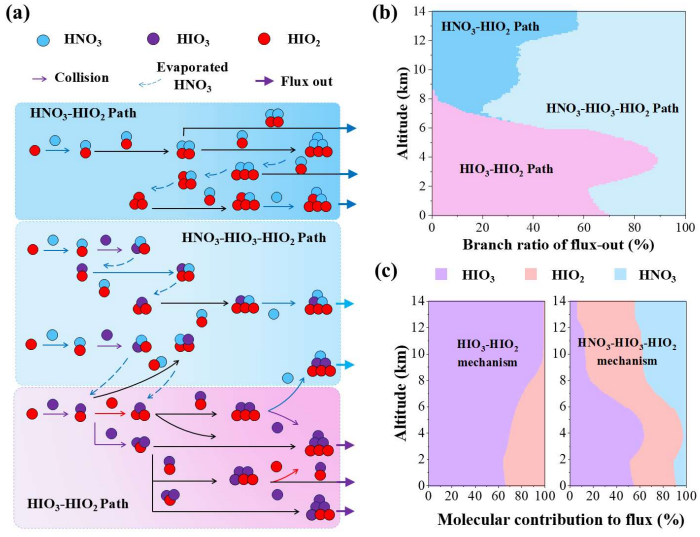


**Figure 5.** Altitude-dependent nucleation pathways and cluster composition under atmospheric conditions in Figure 4. (a) Three primary nucleation pathways identified by ACDC simulations: binary $HIO_3$–$HIO_2$, ternary $HNO_3$–$HIO_3$–$HIO_2$, and binary $HNO_3$–$HIO_2$ pathway. (b) Branching ratios of the flux out for three nucleation pathways at different altitudes. (c) Number contributions of $HNO_3$, $HIO_3$, and $HIO_2$ molecules to the total outflux clusters at different altitudes. Left: $HIO_3$–$HIO_2$ mechanism; Right: $HNO_3$–$HIO_3$–$HIO_2$ mechanism.

### 3.5 Comparison with Typical Nucleation Systems

To assess the atmospheric significance of the proposed $HNO_3$–$HIO_3$–$HIO_2$ mechanism and identify the specific environments where it plays a role, we compared it against well-established nucleation mechanisms. We selected four representative environments: a polluted coastal area (Zhejiang, China), a clean marine site (Mace Head, Ireland), a polar region (Greenland), and UT, encompassing pollution gradients (polluted-to-clean) and temperature ranges (high-to-low) to cover the core application scenarios of the nucleation mechanism. The comparison analysis included three key mechanisms: (1) the binary $HIO_3$–$HIO_2$ nucleation (purple dashed line, as a baseline), (2) the ternary $HNO_3$–$HIO_3$–$HIO_2$ nucleation proposed in this study (blue solid and dashed lines), and (3) the competing $H_2SO_4$-driven mechanism (i.e., $H_2SO_4$–DMA (Kürten et al., 2013) for polluted coastal regions or $H_2SO_4$–$NH_3$–$HNO_3$ for the UT (Wang et al., 2022)) (red solid line). All data (Liu et al., 2018, 2021, 2023) related to quantum chemical calculations of the mechanisms were re-calculated at the same level of theory to ensure the result comparability.

For the polluted coastal environment of Zhejiang (Figure 6(a), 288 K, CS = $1.0 \times 10^{-2}$ $s^{-1}$ (Ning et al., 2022), [$HIO_3$] = $5\times10^6$ molecules $cm^{-3}$ (He et al., 2021),) $HNO_3$ at the typical concentration (Xu et al., 2018) of $1\times10^{10}$ molecules $cm^{-3}$ can

https://doi.org/10.5194/egusphere-2026-1771
Preprint. Discussion started: 20 April 2026


enhance $HIO_3$–$HIO_2$ nucleation by 10-fold, consistent with its catalytic role in the MBL. Under extremely polluted conditions ([$HNO_3$] = $1\times10^{11}$ molecules $cm^{-3}$), this enhancement reaches $10^2$-fold, enabling the $HNO_3$–$HIO_3$–$HIO_2$ mechanism to achieve better agreement with field observations (Yu et al., 2019) (gray shaded area in Figure 6(a)). With ongoing global sulfur emission reductions, the $HNO_3$–$HIO_3$–$HIO_2$ mechanism emerges as an increasingly significant, and potentially dominant, pathway for NPF in polluted coastal regions. At the clean coastal site of Mace Head (Figure 6b, 288 K, CS = $2.0 \times 10^{-3}$ $s^{-1}$) (Sipilä et al., 2016), elevated ambient [$HIO_3$] (Heard et al., 2006) limits $HNO_3$'s contribution, leading to modest enhancement (<1.5-fold). Both $HNO_3$-$HIO_3$-$HIO_2$ and $HIO_3$-$HIO_2$ mechanisms are consistent with the upper limit of field-observed cluster formation rates.

With decreasing temperature or increasing altitude, the enhancement effect of $HNO_3$ on $HIO_3$–$HIO_2$ nucleation becomes progressively pronounced. In the cold polar environment of Greenland (Figure 6(c), 268K, CS = $1.0 \times 10^{-4}$ $s^{-1}$), an [$HIO_3$] of $10^6$–$10^7$ (Baccarini et al., 2020), $HNO_3$ can provide an enhancement of ~2–3 times at typical ambient $HNO_3$ concentrations (e.g., $10^9$ molecules $cm^{-3}$) (Honrath et al., 2002). However, with increasing anthropogenic $NO_x$ emissions from shipping activities due to Arctic warming (Dalsøren et al., 2013; Gong et al., 2018; Qi et al., 2024), local $HNO_3$ concentrations may rise significantly. Our simulations show that if local [$HNO_3$] reaches $10^{10}$ molecules $cm^{-3}$, the cluster formation rate of the $HNO_3$-$HIO_3$-$HIO_2$ mechanism can reach up to $10^2$–$10^4$ $cm^{-3}$ $s^{-1}$, an enhancement of 20-fold compared to the binary $HIO_3$-$HIO_2$ mechanism. This significant enhancement highlights the potential importance of this mechanism for local NPF under the influence of high concentrations of anthropogenic $NO_x$.

In the UT (Figure 6(d), 228 K, CS = $1.0 \times 10^{-4}$ $s^{-1}$) (Williamson et al., 2019), conventional pathways (e.g., pure $HIO_3$–$HIO_2$ nucleation) are inefficient ($10^{-3}$ $cm^{-3}$ $s^{-1}$ < $J$ < $10^2$ $cm^{-3}$ $s^{-1}$). However, at the observed $HNO_3$ concentrations in the UT (~ppb levels, i.e., [$HNO_3$] = $5\times10^9$ molecules $cm^{-3}$) (Jurkat et al., 2014), $J$ increases to $10^3$–$10^4$ $cm^{-3}$ $s^{-1}$, an enhancement of $10^2$ to $10^6$ times over the pure $HIO_3$–$HIO_2$ mechanism, solidifying $HIO_3$'s role as a UT nucleation core component. This rate far exceeds that of the reported $H_2SO_4$–$NH_3$–$HNO_3$ mechanism in this region (1–100 $cm^{-3}$ $s^{-1}$), establishing $HNO_3$–$HIO_3$–$HIO_2$ nucleation as the potentially critical nucleation pathway in the UT, supported by the enhanced stability of $HNO_3$–$HIO_2$ clusters at low temperatures (Tables S3 and S4).

In summary, the enhancement of $HIO_3$–$HIO_2$ nucleation by $HNO_3$ is widespread across diverse atmospheric environments, and it emerges as a potentially dominant mechanism under high–altitude or low–temperature conditions, consistent with its altitude-dependent functional transition from MBL catalyst to UT core component. In the context of $SO_2$ emission reductions, the high atmospheric abundance and broad spatial distribution of $HNO_3$ are anticipated to exert a profound and far-reaching impact on global NPF, highlighting the need to incorporate its altitude-dependent role into atmospheric models.

https://doi.org/10.5194/egusphere-2026-1771
Preprint. Discussion started: 20 April 2026


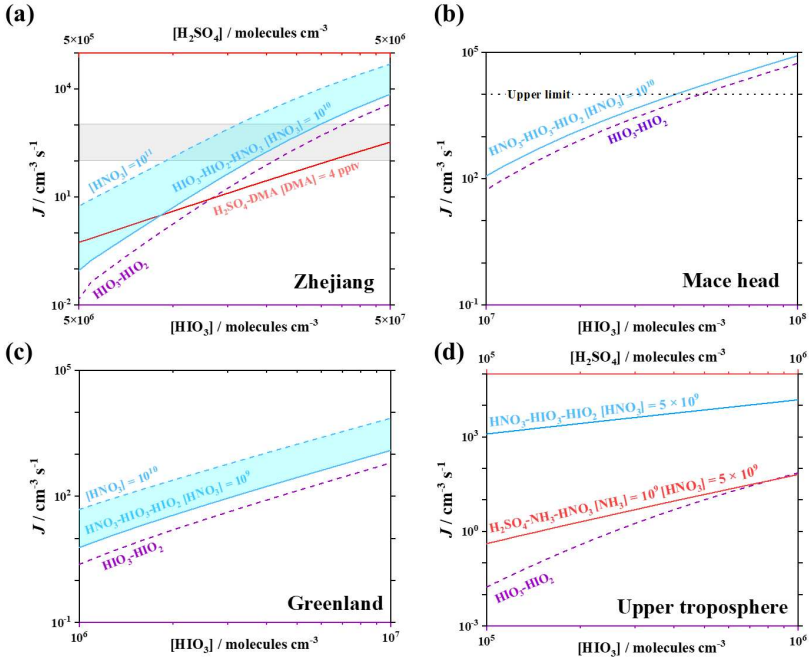


**Figure 6.** Cluster formation rates ($J$, $cm^{-3}$ $s^{-1}$) for $HIO_3$–$HIO_2$ (purple dashed line), $HNO_3$-$HIO_3$-$HIO_2$–(blue) and $H_2SO_4$-DMA or $H_2SO_4$-$NH_3$-$HNO_3$ (red) systems under the corresponding atmospheric conditions in (a) Zhejiang, where gray shaded areas represent locally observed cluster formation rates (Yu et al., 2019); (b) Mace Head, where the dashed line marks the upper limit of cluster formation rates reported in field observations (Sipilä et al., 2016); (c) Greenland; and (d) the UT.

### 3.6 Uncertainty Analysis

To evaluate the robustness of our results, specifically $HNO_3$'s altitude-dependent transition from MBL catalyst to UT core component, we systematically analyzed uncertainties arising from two primary sources: quantum chemical calculations of Gibbs free energies of cluster formation ($\Delta G$) and the atmospheric constraints on precursor concentrations ($HIO_3$ and $HIO_2$).

Regarding quantum chemical calculations, we examined the sensitivity of $J$ to calculated $\Delta G$ variations by applying ±1 kcal $mol^{-1}$ perturbations to all clusters (Figure S6), a magnitude consistent with prior benchmarks showing that DLPNO-CCSD(T) typically exhibits a potential $\Delta E$ error of < 1 kcal $mol^{-1}$ relative to CCSD(F12*)/CBS results (Schmitz and Elm, 2020). These perturbations directly affect cluster stability: a +1 kcal $mol^{-1}$ shift destabilizes clusters and increases evaporation rates into monomers, while a -1 kcal $mol^{-1}$ shift enhances stabilization against evaporation (evaporation rate coefficient $\gamma$ in eq S2). Under MBL conditions, where $HNO_3$ acts primarily as a catalyst and cluster evaporation is inherently rapid, these perturbations significantly affect the enhancement factor ($R$) of $HNO_3$: +1 kcal $mol^{-1}$ shift reduces $R$ to < 2, while -1 kcal $mol^{-1}$

https://doi.org/10.5194/egusphere-2026-1771
Preprint. Discussion started: 20 April 2026


[1] shift increases it to > 10 (baseline $R$ = 2–3). Notably, this sensitivity diminishes rapidly with the increasing altitude. In the UT, where $HNO_3$ serves as a core component and its evaporation is effectively suppressed, the impact of $\Delta G$ perturbations on $J$ becomes negligible. This altitude-dependent sensitivity not only validates $HNO_3$'s functional transition (from MBL catalyst to UT core component), but also confirms its robust enhancement at high altitudes.

We further conducted sensitivity tests for the concentrations of $HIO_3$ and $HIO_2$ (Figures S7 and S8) to assess the mechanism's applicability across varying atmospheric conditions. Consistent with the flux composition (Figure 5(c)), the $HNO_3$–$HIO_3$–$HIO_2$ mechanism shows strong sensitivity to $HIO_2$ concentrations: $HNO_3$ enhances nucleation even at low [$HIO_2$], both $J$ and $R$ increase substantially with $HIO_2$ abundance. Although atmospheric $HIO_2$ concentrations remain poorly constrained, our simulated concentration ranges are consistent with CLOUD chamber observations under UT conditions (Shen et al., 2024). Furthermore, theoretical studies have confirmed $HIO_2$'s stability against tropospheric photolysis (De Souza and Brown, 2014) and oxidation (Khanniche et al., 2017), supporting the mechanism's robustness under realistic conditions.

## 4 Conclusion

This study combines quantum chemical calculations and ACDC simulations, to elucidate the role of $HNO_3$ in iodine oxoacid nucleation, establishing an altitude-dependent $HNO_3$–$HIO_3$–$HIO_2$ nucleation mechanism. Specifically, at the molecular level, $HNO_3$ can stabilize $HIO_3$-$HIO_2$ clusters through a network of hydrogen bonding, halogen bonding, and proton transfer-driven electrostatic interactions. Thermodynamically, the stability of $HNO_3$-containing clusters exhibits a strong temperature dependence and increases significantly with decreasing temperature, which directly drives the altitude-dependent functional transition of $HNO_3$. Kinetically, the $J$ shows a non-monotonic vertical profile governed by temperature, CS, and precursor concentrations.

In the low-altitude MBL, high temperatures drive rapid cluster evaporation, thus restricting $HNO_3$ to a catalytic role via a collision-re-evaporation cycles that confers modest $J$ enhancement (~1.5–2-fold). In the UT, low temperatures strongly suppress evaporation, allowing $HNO_3$ to serve as a core cluster component. This shift leads to the dominance of $HNO_3$–involved pathways and boosts the nucleation rate by up to 200-fold relative to the binary $HIO_3$–$HIO_2$ mechanism, reaching $10^3$–$10^4$ $cm^{-3}$ $s^{-1}$ in the UT, exceeding the classic $H_2SO_4$–$NH_3$–$HNO_3$ nucleation pathway.

The proposed $HNO_3$-$HIO_3$-$HIO_2$ nucleation mechanism provides a new theoretical perspective for interpreting the intense NPF events in both polluted coastal regions and the upper troposphere. It grows in importance as global sulfur emissions decline, while also becoming relevant to rapid NPF in the Arctic under increasing anthropogenic nitrogen emissions. By mediating iodine nucleation across the troposphere, $HNO_3$ effectively links marine iodine emissions to troposphere-wide CCN production, with implications for cloud formation and Earth's radiative balance.

These findings highlight the critical need to incorporate altitude-dependent $HNO_3$–iodine nucleation into global climate and aerosol models. Future work should explore interactions with other atmospheric bases (e.g., ammonia, amines) and acids

https://doi.org/10.5194/egusphere-2026-1771
Preprint. Discussion started: 20 April 2026


(e.g., organic acids, methanesulfonic acid), as well as joint laboratory, field, and modeling studies, to further constrain the role of $HNO_3$ in complex atmospheric environments.

**Data availability**

The data in this article are available from the corresponding author upon reasonable request (lingliu@bit.edu.cn and zhangxiuhui@bit.edu.cn).

**Author contributions**

XZ designed and supervised the research. JZ, LL and HZ performed the quantum chemical calculations and the ACDC simulations. LL, AN and XZ analyzed data. JZ, LL and XZ wrote the manuscript. HZ, JL, FB and JY, reviewed and edited the manuscript. All authors commented on the paper.

**Competing interests**

The contact author has declared that neither they nor their co-authors have any competing interests.

**Disclaimer**

Publisher's note: Copernicus Publications remains neutral with regard to jurisdictional claims in published maps and institutional affiliations.

**Acknowledgements**

This work was supported by the National Science Fund for Distinguished Young Scholars [grant number 22225607] and the National Natural Science Foundation of China [grant numbers 22376013 and 22306011]. L. Liu thanks the Beijing Institute of Technology Research Fund Program for Young Scholars. We thank for the technical support of the National Large Scientific and Technological Infrastructure "Earth System Numerical Simulation Facility" (https://cstr.cn/31134.02.EL).

https://doi.org/10.5194/egusphere-2026-1771
Preprint. Discussion started: 20 April 2026


**Financial support**

This work was supported by the National Science Fund for Distinguished Young Scholars [grant number 22225607] and the National Natural Science Foundation of China [grant numbers 22376013 and 22306011]. L. Liu thanks the Beijing Institute of Technology Research Fund Program for Young Scholars.

## References

Aas, W., Mortier, A., Bowersox, V., Cherian, R., Faluvegi, G., Fagerli, H., Hand, J., Klimont, Z., Galy-Lacaux, C., Lehmann, C. M. B., Myhre, C. L., Myhre, G., Olivié, D., Sato, K., Quaas, J., Rao, P. S. P., Schulz, M., Shindell, D., Skeie, R. B., Stein, A., Takemura, T., Tsyro, S., Vet, R., and Xu, X.: Global and regional trends of atmospheric sulfur, Sci. Rep., 9, 953, https://doi.org/10.1038/s41598-018-37304-0, 2019.

Acker, K., Möller, D., Auel, R., Wieprecht, W., and Kalaß, D.: Concentrations of nitrous acid, nitric acid, nitrite and nitrate in the gas and aerosol phase at a site in the emission zone during ESCOMPTE 2001 experiment, Atmos. Res., 74, 507–524, https://doi.org/10.1016/j.atmosres.2004.04.009, 2005.

Baccarini, A., Karlsson, L., Dommen, J., Duplessis, P., Vüllers, J., Brooks, I. M., Saiz-Lopez, A., Salter, M., Tjernström, M., Baltensperger, U., Zieger, P., and Schmale, J.: Frequent new particle formation over the high Arctic pack ice by enhanced iodine emissions, Nat Commun, 11, 4924, https://doi.org/10.1038/s41467-020-18551-0, 2020.

Bai, X., Lian, Y., Peng, J., Mao, H., and Jiang, S.: Ethylenediamine-Enhanced Iodic Acid Nucleation: Mechanistic Insights into Marine New Particle Formation, Environ. Sci. Technol., 59, 22772–22783, https://doi.org/10.1021/acs.est.5c08562, 2025.

Catling, D. C. and Kasting, J. F.: Atmospheric Evolution on Inhabited and Lifeless Worlds, Cambridge University Press, 595 pp., 2017.

Chan, B. and Yim, W.-L.: Accurate Computation of Cohesive Energies for Small to Medium-Sized Gold Clusters, J. Chem. Theory Comput., 9, 1964–1970, https://doi.org/10.1021/ct400047y, 2013.

Cuevas, C. A., Maffezzoli, N., Corella, J. P., Spolaor, A., Vallelonga, P., Kjær, H. A., Simonsen, M., Winstrup, M., Vinther, B., Horvat, C., Fernandez, R. P., Kinnison, D., Lamarque, J.-F., Barbante, C., and Saiz-Lopez, A.: Rapid increase in atmospheric iodine levels in the North Atlantic since the mid-20th century, Nat Commun, 9, 1452, https://doi.org/10.1038/s41467-018-03756-1, 2018.

Dalsøren, S. B., Samset, B. H., Myhre, G., Corbett, J. J., Minjares, R., Lack, D., and Fuglestvedt, J. S.: Environmental impacts of shipping in 2030 with a particular focus on the Arctic region, Atmos. Chem. Phys., 13, 1941–1955, https://doi.org/10.5194/acp-13-1941-2013, 2013.

De Souza, G. L. C. and Brown, A.: Probing ground and low-lying excited states for $HIO_2$ isomers, J. Chem. Phys., 141, 234303, https://doi.org/10.1063/1.4903789, 2014.

Dunne, E. M., Gordon, H., Kürten, A., Almeida, J., Duplissy, J., Williamson, C., Ortega, I. K., Pringle, K. J., Adamov, A., Baltensperger, U., Barmet, P., Benduhn, F., Bianchi, F., Breitenlechner, M., Clarke, A., Curtius, J., Dommen, J., Donahue, N.

https://doi.org/10.5194/egusphere-2026-1771
Preprint. Discussion started: 20 April 2026


M., Ehrhart, S., Flagan, R. C., Franchin, A., Guida, R., Hakala, J., Hansel, A., Heinritzi, M., Jokinen, T., Kangasluoma, J., Kirkby, J., Kulmala, M., Kupc, A., Lawler, M. J., Lehtipalo, K., Makhmutov, V., Mann, G., Mathot, S., Merikanto, J., Miettinen, P., Nenes, A., Onnela, A., Rap, A., Reddington, C. L. S., Riccobono, F., Richards, N. A. D., Rissanen, M. P., Rondo, L., Sarnela, N., Schobesberger, S., Sengupta, K., Simon, M., Sipilä, M., Smith, J. N., Stozkhov, Y., Tomé, A., Tröstl, J., Wagner, P. E., Wimmer, D., Winkler, P. M., Worsnop, D. R., and Carslaw, K. S.: Global atmospheric particle formation from CERN CLOUD measurements, Science, 354, 1119–1124, https://doi.org/10.1126/science.aaf2649, 2016.

Emamian, S., Lu, T., Kruse, H., and Emamian, H.: Exploring Nature and Predicting Strength of Hydrogen Bonds: A Correlation Analysis Between Atoms-in-Molecules Descriptors, Binding Energies, and Energy Components of Symmetry-Adapted Perturbation Theory, J. Comput. Chem., 40, 2868–2881, https://doi.org/10.1002/jcc.26068, 2019.

Fan, J., Wang, Y., Rosenfeld, D., and Liu, X.: Review of Aerosol–Cloud Interactions: Mechanisms, Significance, and Challenges, J. Atmos. Sci., 73, 4221–4252, https://doi.org/10.1175/JAS-D-16-0037.1, 2016.

Finkenzeller, H., Iyer, S., He, X.-C., Simon, M., Koenig, T. K., Lee, C. F., Valiev, R., Hofbauer, V., Amorim, A., Baalbaki, R., Baccarini, A., Beck, L., Bell, D. M., Caudillo, L., Chen, D., Chiu, R., Chu, B., Dada, L., Duplissy, J., Heinritzi, M., Kemppainen, D., Kim, C., Krechmer, J., Kürten, A., Kvashnin, A., Lamkaddam, H., Lee, C. P., Lehtipalo, K., Li, Z., Makhmutov, V., Manninen, H. E., Marie, G., Marten, R., Mauldin, R. L., Mentler, B., Müller, T., Petäjä, T., Philippov, M., Ranjithkumar, A., Rörup, B., Shen, J., Stolzenburg, D., Tauber, C., Tham, Y. J., Tomé, A., Vazquez-Pufleau, M., Wagner, A. C., Wang, D. S., Wang, M., Wang, Y., Weber, S. K., Nie, W., Wu, Y., Xiao, M., Ye, Q., Zauner-Wieczorek, M., Hansel, A., Baltensperger, U., Brioude, J., Curtius, J., Donahue, N. M., Haddad, I. E., Flagan, R. C., Kulmala, M., Kirkby, J., Sipilä, M., Worsnop, D. R., Kurten, T., Rissanen, M., and Volkamer, R.: The gas-phase formation mechanism of iodic acid as an atmospheric aerosol source, Nat. Chem., 15, 129–135, https://doi.org/10.1038/s41557-022-01067-z, 2023.

Francl, M. M., Pietro, W. J., Hehre, W. J., Binkley, J. S., Gordon, M. S., DeFrees, D. J., and Pople, J. A.: Self-consistent molecular orbital methods. XXIII. A polarization-type basis set for second-row elements, J. Chem. Phys., 77, 3654–3665, https://doi.org/10.1063/1.444267, 1982.

Frege, C., Bianchi, F., Molteni, U., Tröstl, J., Junninen, H., Henne, S., Sipilä, M., Herrmann, E., Rossi, M. J., Kulmala, M., Hoyle, C. R., Baltensperger, U., and Dommen, J.: Chemical characterization of atmospheric ions at the high altitude research station Jungfraujoch (Switzerland), Atmos. Chem. Phys., 17, 2613–2629, https://doi.org/10.5194/acp-17-2613-2017, 2017.

Frisch, M. J., Trucks, G. W., Schlegel, H. B., Scuseria, G. E., Robb, M. A., Cheeseman, J. R., Scalmani, G., Barone, V., Mennucci, B., Petersson, G. A., Nakatsuji, H., Caricato, M., Li, X., Hratchian, H. P., Izmaylov, A. F., Bloino, J., Zheng, G., Sonnenberg, J. L., Hada, M., E., M., Toyota, K., Fukuda, R., Hasegawa, J., Ishida, M., Nakajima, T., Honda, Y., Kitao, O., Nakai, H., Vreven, T., Montgomery, J. A., Peralta, J. E., Ogliaro, F., Bearpark, M., Heyd, J. J., Brothers, E., Kudin, K. N., Staroverov, V. N., Kobayashi, R., Normand, J., Raghavachari, K., Rendell, A., Burant, J. C., Iyengar, S. S., Tomasi, J., Cossi, M., Rega, N., Millam, J. M., Klene, M., Knox, J. E., Cross, J. B., Bakken, V., Adamo, C., Jaramillo, J., Gomperts, R., Stratmann, R. E., Yazyev, O., Austin, A. J., Cammi, R., Pomelli, C., Ochterski, J. W., Martin, R. L., Morokuma, K., Zakrzewski, V. G., Voth, G. A., Salvador, P., Dannenberg, J. J., Dapprich, S., Daniels, A. D., Farkas, O., Foresman, J. B., Ortiz, J. V., Cioslowski,

https://doi.org/10.5194/egusphere-2026-1771
Preprint. Discussion started: 20 April 2026


J., and Fox, D. J.: Gaussian 09, Revision A.02; Gaussian, Inc.: Wallingford CT, https://gaussian.com/g09citation/ (last access: 19 March 2026), 2009.

Frisch, M. J., Trucks, G. W., Schlegel, H. B., Scuseria, G. E., Robb, M. A., Cheeseman, J. R., Scalmani, G., Barone, V., Mennucci, B., Petersson, G. A., Nakatsuji, H., Caricato, M., Li, X., Hratchian, H. P., Izmaylov, A. F., Bloino, J., Zheng, G., Sonnenberg, J. L., Hada, M., Ehara, M., Toyota, K., Fukuda, R., Hasegawa, J., Ishida, M., Nakajima, T., Honda, Y., Kitao, O., Nakai, H., Vreven, T., Montgomery, J. A., Peralta, J. E., Ogliaro, F., Bearpark, M., Heyd, J. J., Brothers, E., Kudin, K. N., Staroverov, V. N., Kobayashi, R., Normand, J., Raghavachari, K., Rendell, A., Burant, J. C., Iyengar, S. S., Tomasi, J., Cossi, M., Rega, N., Millam, J. M., Klene, M., Knox, J. E., Cross, J. B., Bakken, V., Adamo, C., Jaramillo, J., Gomperts, R., Stratmann, R. E., Yazyev, O., Austin, A. J., Cammi, R., Pomelli, C., Ochterski, J. W., Martin, R. L., Morokuma, K., Zakrzewski, V. G., Voth, G. A., Salvador, P., Dannenberg, J. J., Dapprich, S., Daniels, A. D., Farkas, O., Foresman, J. B., Ortiz, J. V., Cioslowski, J., and Fox, D. J.: Gaussian 16, Revision A.03; Gaussian, Inc.: Wallingford CT, https://gaussian.com/citation_a03/ (last access: 19 March 2026), 2016.

Gong, W., Beagley, S. R., Cousineau, S., Sassi, M., Munoz-Alpizar, R., Ménard, S., Racine, J., Zhang, J., Chen, J., Morrison, H., Sharma, S., Huang, L., Bellavance, P., Ly, J., Izdebski, P., Lyons, L., and Holt, R.: Assessing the impact of shipping emissions on air pollution in the Canadian Arctic and northern regions: current and future modelled scenarios, Atmos. Chem. Phys., 18, 16653–16687, https://doi.org/10.5194/acp-18-16653-2018, 2018.

Gordon, H., Kirkby, J., Baltensperger, U., Bianchi, F., Breitenlechner, M., Curtius, J., Dias, A., Dommen, J., Donahue, N. M., Dunne, E. M., Duplissy, J., Ehrhart, S., Flagan, R. C., Frege, C., Fuchs, C., Hansel, A., Hoyle, C. R., Kulmala, M., Kürten, A., Lehtipalo, K., Makhmutov, V., Molteni, U., Rissanen, M. P., Stozkhov, Y., Tröstl, J., Tsagkogeorgas, G., Wagner, R., Williamson, C., Wimmer, D., Winkler, P. M., Yan, C., and Carslaw, K. S.: Causes and importance of new particle formation in the present-day and preindustrial atmospheres, JGR Atmospheres, 122, 8739–8760, https://doi.org/10.1002/2017JD026844, 2017.

Halonen, R., Zapadinsky, E., Kurtén, T., Vehkamäki, H., and Reischl, B.: Rate enhancement in collisions of sulfuric acid molecules due to long-range intermolecular forces, Atmos. Chem. Phys., 19, 13355–13366, https://doi.org/10.5194/acp-19-13355-2019, 2019.

Haywood, J. and Boucher, O.: Estimates of the direct and indirect radiative forcing due to tropospheric aerosols: A review, Rev. Geophys., 38, 513–543, https://doi.org/10.1029/1999RG000078, 2000.

He, X.-C., Tham, Y. J., Dada, L., Wang, M., Finkenzeller, H., Stolzenburg, D., Iyer, S., Simon, M., Kürten, A., Shen, J., Rörup, B., Rissanen, M., Schobesberger, S., Baalbaki, R., Wang, D. S., Koenig, T. K., Jokinen, T., Sarnela, N., Beck, L. J., Almeida, J., Amanatidis, S., Amorim, A., Ataei, F., Baccarini, A., Bertozzi, B., Bianchi, F., Brilke, S., Caudillo, L., Chen, D., Chiu, R., Chu, B., Dias, A., Ding, A., Dommen, J., Duplissy, J., El Haddad, I., Gonzalez Carracedo, L., Granzin, M., Hansel, A., Heinritzi, M., Hofbauer, V., Junninen, H., Kangasluoma, J., Kemppainen, D., Kim, C., Kong, W., Krechmer, J. E., Kvashin, A., Laitinen, T., Lamkaddam, H., Lee, C. P., Lehtipalo, K., Leiminger, M., Li, Z., Makhmutov, V., Manninen, H. E., Marie, G., Marten, R., Mathot, S., Mauldin, R. L., Mentler, B., Möhler, O., Müller, T., Nie, W., Onnela, A., Petäjä, T., Pfeifer, J., Philippov, M.,

https://doi.org/10.5194/egusphere-2026-1771
Preprint. Discussion started: 20 April 2026


Ranjithkumar, A., Saiz-Lopez, A., Salma, I., Scholz, W., Schuchmann, S., Schulze, B., Steiner, G., Stozhkov, Y., Tauber, C., Tomé, A., Thakur, R. C., Väisänen, O., Vazquez-Pufleau, M., Wagner, A. C., Wang, Y., Weber, S. K., Winkler, P. M., Wu, Y., Xiao, M., Yan, C., Ye, Q., Ylisirniö, A., Zauner-Wieczorek, M., Zha, Q., Zhou, P., Flagan, R. C., Curtius, J., Baltensperger, U., Kulmala, M., Kerminen, V.-M., Kurtén, T., et al.: Role of iodine oxoacids in atmospheric aerosol nucleation, Science, 371, 589–595, https://doi.org/10.1126/science.abe0298, 2021.

He, X.-C., Simon, M., Iyer, S., Xie, H.-B., Rörup, B., Shen, J., Finkenzeller, H., Stolzenburg, D., Zhang, R., Baccarini, A., Tham, Y. J., Wang, M., Amanatidis, S., Piedehierro, A. A., Amorim, A., Baalbaki, R., Brasseur, Z., Caudillo, L., Chu, B., Dada, L., Duplissy, J., El Haddad, I., Flagan, R. C., Granzin, M., Hansel, A., Heinritzi, M., Hofbauer, V., Jokinen, T., Kemppainen, D., Kong, W., Krechmer, J., Kürten, A., Lamkaddam, H., Lopez, B., Ma, F., Mahfouz, N. G. A., Makhmutov, V., Manninen, H. E., Marie, G., Marten, R., Massabò, D., Mauldin, R. L., Mentler, B., Onnela, A., Petäjä, T., Pfeifer, J., Philippov, M., Ranjithkumar, A., Rissanen, M. P., Schobesberger, S., Scholz, W., Schulze, B., Surdu, M., Thakur, R. C., Tomé, A., Wagner, A. C., Wang, D., Wang, Y., Weber, S. K., Welti, A., Winkler, P. M., Zauner-Wieczorek, M., Baltensperger, U., Curtius, J., Kurtén, T., Worsnop, D. R., Volkamer, R., Lehtipalo, K., Kirkby, J., Donahue, N. M., Sipilä, M., and Kulmala, M.: Iodine oxoacids enhance nucleation of sulfuric acid particles in the atmosphere, Science, 382, 1308–1314, https://doi.org/10.1126/science.adh2526, 2023.

Heard, D. E., Read, K. A., Methven, J., Al-Haider, S., Bloss, W. J., Johnson, G. P., Pilling, M. J., Seakins, P. W., Smith, S. C., Sommariva, R., Stanton, J. C., Still, T. J., Ingham, T., Brooks, B., Leeuw, G. D., Jackson, A. V., McQuaid, J. B., Morgan, R., Smith, M. H., Carpenter, L. J., Carslaw, N., Hamilton, J., Hopkins, J. R., Lee, J. D., Lewis, A. C., Purvis, R. M., Wevill, D. J., Brough, N., Green, T., Mills, G., Penkett, S. A., Plane, J. M. C., Saiz-Lopez, A., Worton, D., Monks, P. S., Fleming, Z., Rickard, A. R., Alfarra, M. R., Allan, J. D., Bower, K., Coe, H., Cubison, M., Flynn, M., McFiggans, G., Gallagher, M., Norton, E. G., O'Dowd, C. D., Shillito, J., Topping, D., Vaughan, G., Williams, P., Bitter, M., Ball, S. M., Jones, R. L., Povey, I. M., O'Doherty, S., Simmonds, P. G., Allen, A., Kinnersley, R. P., Beddows, D. C. S., Dall'Osto, M., Harrison, R. M., Donovan, R. J., Heal, M. R., Jennings, S. G., Noone, C., and Spain, G.: The North Atlantic Marine Boundary Layer Experiment (NAMBLEX). Overview of the campaign held at Mace Head, Ireland, in summer 2002, Atmos. Chem. Phys., 6, 2241–2272, https://doi.org/10.5194/acp-6-2241-2006, 2006.

Hirshorn, N. S., Zuromski, L. M., Rapp, C., McCubbin, I., Carrillo-Cardenas, G., Yu, F., and Hallar, A. G.: Seasonal significance of new particle formation impacts on cloud condensation nuclei at a mountaintop location, Atmos. Chem. Phys., 22, 15909–15924, https://doi.org/10.5194/acp-22-15909-2022, 2022.

Holzer, C., Franzke, Y. J., and Pausch, A.: Current density functional framework for spin–orbit coupling, J. Chem. Phys., 157, 204102, https://doi.org/10.1063/5.0122394, 2022.

Honrath, R. E., Lu, Y., Peterson, M. C., Dibb, J. E., Arsenault, M. A., Cullen, N. J., and Steffen, K.: Vertical fluxes of $NO_x$, HONO, and $HNO_3$ above the snowpack at Summit, Greenland, Atmos. Environ., 36, 2629–2640, https://doi.org/10.1016/S1352-2310(02)00132-2, 2002.

Humphrey, W., Dalke, A., and Schulten, K.: VMD: visual molecular dynamics, J. Mol. Graph., 14, 33–38, 1996.

https://doi.org/10.5194/egusphere-2026-1771
Preprint. Discussion started: 20 April 2026


Jones, A. E., Brough, N., Anderson, P. S., and Wolff, E. W.: $HO_2NO_2$ and $HNO_3$ in the coastal Antarctic winter night: a "lab-in-the-field" experiment, Atmos. Chem. Phys., 14, 11843–11851, https://doi.org/10.5194/acp-14-11843-2014, 2014.

Jurkat, T., Voigt, C., Kaufmann, S., Zahn, A., Sprenger, M., Hoor, P., Bozem, H., Müller, S., Dörnbrack, A., Schlager, H., Bönisch, H., and Engel, A.: A quantitative analysis of stratospheric HCl, $HNO_3$, and $O_3$ in the tropopause region near the subtropical jet, Geophys. Res. Lett., 41, 3315–3321, https://doi.org/10.1002/2013GL059159, 2014.

Khanniche, S., Louis, F., Cantrel, L., and Černušák, I.: Thermochemistry of $HIO_2$ Species and Reactivity of Iodous Acid with OH Radical: A Computational Study, ACS Earth Space Chem., 1, 39–49, https://doi.org/10.1021/acsearthspacechem.6b00010, 2017.

Koenig, T. K., Baidar, S., Campuzano-Jost, P., Cuevas, C. A., Dix, B., Fernandez, R. P., Guo, H., Hall, S. R., Kinnison, D., Nault, B. A., Ullmann, K., Jimenez, J. L., Saiz-Lopez, A., and Volkamer, R.: Quantitative detection of iodine in the stratosphere, Proc. Natl. Acad. Sci. U.S.A., 117, 1860–1866, https://doi.org/10.1073/pnas.1916828117, 2020.

Kühn, M. and Weigend, F.: Two-component hybrid time-dependent density functional theory within the Tamm-Dancoff approximation, J. Chem. Phys., 142, 034116, https://doi.org/10.1063/1.4905829, 2015.

Kulmala, M., Kontkanen, J., Junninen, H., Lehtipalo, K., Manninen, H. E., Nieminen, T., Petäjä, T., Sipilä, M., Schobesberger, S., Rantala, P., Franchin, A., Jokinen, T., Järvinen, E., Äijälä, M., Kangasluoma, J., Hakala, J., Aalto, P. P., Paasonen, P., Mikkilä, J., Vanhanen, J., Aalto, J., Hakola, H., Makkonen, U., Ruuskanen, T., Mauldin, R. L., Duplissy, J., Vehkamäki, H., Bäck, J., Kortelainen, A., Riipinen, I., Kurtén, T., Johnston, M. V., Smith, J. N., Ehn, M., Mentel, T. F., Lehtinen, K. E. J., Laaksonen, A., Kerminen, V.-M., and Worsnop, D. R.: Direct Observations of Atmospheric Aerosol Nucleation, Science, 339, 943–946, https://doi.org/10.1126/science.1227385, 2013.

Kürten, A., Ortega, I. K., Kupiainen-Määttä, O., Praplan, A. P., Adamov, A., Amorim, A., Bianchi, F., Breitenlechner, M., David, A., Dommen, J., Donahue, N. M., Downard, A., Dunne, E., Duplissy, J., Ehrhart, S., Flagan, R. C., Franchin, A., Guida, R., Hakala, J., Hansel, A., Heinritzi, M., Henschel, H., Jokinen, T., Junninen, H., Kajos, M., Kangasluoma, J., Keskinen, H., Kupc, A., Kurtén, T., Kvashin, A. N., Laaksonen, A., Lehtipalo, K., Leiminger, M., Leppä, J., Loukonen, V., Makhmutov, V., Mathot, S., McGrath, M. J., Nieminen, T., Olenius, T., Onnela, A., Petäjä, T., Riccobono, F., Riipinen, I., Rissanen, M., Rondo, L., Ruuskanen, T., Santos, F. D., Sarnela, N., Schallhart, S., Schnitzhofer, R., Seinfeld, J. H., Simon, M., Sipilä, M., Stozhkov, Y., Stratmann, F., Tomé, A., Tröstl, J., Tsagkogeorgas, G., Vaattovaara, P., Viisanen, Y., Virtanen, A., Vrtala, A., Wagner, P. E., Weingartner, E., Wex, H., Williamson, C., Wimmer, D., Ye, P., Yli-Juuti, T., Carslaw, K. S., Kulmala, M., Curtius, J., Baltensperger, U., Worsnop, D. R., Vehkamäki, H., and Kirkby, J.: Molecular understanding of sulphuric acid–amine particle nucleation in the atmosphere, Nature, 502, 359–363, https://doi.org/10.1038/nature12663, 2013.

Lane, J. R., Contreras-García, J., Piquemal, J.-P., Miller, B. J., and Kjaergaard, H. G.: Are Bond Critical Points Really Critical for Hydrogen Bonding?, J. Chem. Theory Comput., 9, 3263–3266, https://doi.org/10.1021/ct400420r, 2013.

Legrand, M., McConnell, J. R., Preunkert, S., Arienzo, M., Chellman, N., Gleason, K., Sherwen, T., Evans, M. J., and Carpenter, L. J.: Alpine ice evidence of a three-fold increase in atmospheric iodine deposition since 1950 in Europe due to

https://doi.org/10.5194/egusphere-2026-1771
Preprint. Discussion started: 20 April 2026


increasing oceanic emissions, Proc. Natl. Acad. Sci. U.S.A., 115, 12136–12141, https://doi.org/10.1073/pnas.1809867115, 2018.

Lehtinen, K. E. J., Dal Maso, M., Kulmala, M., and Kerminen, V.-M.: Estimating nucleation rates from apparent particle formation rates and vice versa: Revised formulation of the Kerminen–Kulmala equation, J. Aerosol Sci., 38, 988–994, https://doi.org/10.1016/j.jaerosci.2007.06.009, 2007.

Lehtipalo, K., Rondo, L., Kontkanen, J., Schobesberger, S., Jokinen, T., Sarnela, N., Kürten, A., Ehrhart, S., Franchin, A., Nieminen, T., Riccobono, F., Sipilä, M., Yli-Juuti, T., Duplissy, J., Adamov, A., Ahlm, L., Almeida, J., Amorim, A., Bianchi, F., Breitenlechner, M., Dommen, J., Downard, A. J., Dunne, E. M., Flagan, R. C., Guida, R., Hakala, J., Hansel, A., Jud, W., Kangasluoma, J., Kerminen, V.-M., Keskinen, H., Kim, J., Kirkby, J., Kupc, A., Kupiainen-Määttä, O., Laaksonen, A., Lawler, M. J., Leiminger, M., Mathot, S., Olenius, T., Ortega, I. K., Onnela, A., Petäjä, T., Praplan, A., Rissanen, M. P., Ruuskanen, T., Santos, F. D., Schallhart, S., Schnitzhofer, R., Simon, M., Smith, J. N., Tröstl, J., Tsagkogeorgas, G., Tomé, A., Vaattovaara, P., Vehkamäki, H., Vrtala, A. E., Wagner, P. E., Williamson, C., Wimmer, D., Winkler, P. M., Virtanen, A., Donahue, N. M., Carslaw, K. S., Baltensperger, U., Riipinen, I., Curtius, J., Worsnop, D. R., and Kulmala, M.: The effect of acid–base clustering and ions on the growth of atmospheric nano-particles, Nat Commun, 7, 11594, https://doi.org/10.1038/ncomms11594, 2016.

Li, J., Carlson, B. E., Yung, Y. L., Lv, D., Hansen, J., Penner, J. E., Liao, H., Ramaswamy, V., Kahn, R. A., Zhang, P., Dubovik, O., Ding, A., Lacis, A. A., Zhang, L., and Dong, Y.: Scattering and absorbing aerosols in the climate system, Nat Rev Earth Environ, 3, 363–379, https://doi.org/10.1038/s43017-022-00296-7, 2022.

Li, J., Ning, A., Liu, L., and Zhang, X.: Atmospheric Bases-Enhanced Iodic Acid Nucleation: Altitude-Dependent Characteristics and Molecular Mechanisms, Environ. Sci. Technol., 58, 16962–16973, https://doi.org/10.1021/acs.est.4c06053, 2024a.

Li, J., Ning, A., Liu, L., and Zhang, X.: Atmospheric Bases-Enhanced Iodic Acid Nucleation: Altitude-Dependent Characteristics and Molecular Mechanisms, Environ. Sci. Technol., 58, 16962–16973, https://doi.org/10.1021/acs.est.4c06053, 2024b.

Li, J., Wu, N., Chu, B., Ning, A., and Zhang, X.: Molecular-level study on the role of methanesulfonic acid in iodine oxoacid nucleation, Atmos. Chem. Phys., 24, 3989–4000, https://doi.org/10.5194/acp-24-3989-2024, 2024c.

Liu, L., Li, H., Zhang, H., Zhong, J., Bai, Y., Ge, M., Li, Z., Chen, Y., and Zhang, X.: The role of nitric acid in atmospheric new particle formation, Physical Chemistry Chemical Physics, 20, 17406–17414, https://doi.org/10.1039/c8cp02719f, 2018.

Liu, L., Yu, F., Du, L., Yang, Z., Francisco, J. S., and Zhang, X.: Rapid sulfuric acid–dimethylamine nucleation enhanced by nitric acid in polluted regions, Proc. Natl. Acad. Sci. U.S.A., 118, e2108384118, https://doi.org/10.1073/pnas.2108384118, 2021.

Liu, L., Li, S., Zu, H., and Zhang, X.: Unexpectedly significant stabilizing mechanism of iodous acid on iodic acid nucleation under different atmospheric conditions, Sci. Total Environ., 859, 159832, https://doi.org/10.1016/j.scitotenv.2022.159832, 2023.

https://doi.org/10.5194/egusphere-2026-1771
Preprint. Discussion started: 20 April 2026


Lu, T. and Chen, F.: Multiwfn: A multifunctional wavefunction analyzer, J. Comput. Chem., 33, 580–592, https://doi.org/10.1002/jcc.22885, 2012.

Lu, T. and Chen, Q.: Shermo: A general code for calculating molecular thermochemistry properties, Comput. Theor. Chem., 1200, 113249, https://doi.org/10.1016/j.comptc.2021.113249, 2021.

Ma, F., Xie, H.-B., Zhang, R., Su, L., Jiang, Q., Tang, W., Chen, J., Engsvang, M., Elm, J., and He, X.-C.: Enhancement of Atmospheric Nucleation Precursors on Iodic Acid-Induced Nucleation: Predictive Model and Mechanism, Environ. Sci. Technol., 57, 6944–6954, https://doi.org/10.1021/acs.est.3c01034, 2023.

McGrath, M. J., Olenius, T., Ortega, I. K., Loukonen, V., Paasonen, P., Kurtén, T., Kulmala, M., and Vehkamäki, H.: Atmospheric Cluster Dynamics Code: a flexible method for solution of the birth-death equations, Atmos. Chem. Phys., 12, 2345–2355, https://doi.org/10.5194/acp-12-2345-2012, 2012.

Mehra, M., Wang, Y., Ramesh, C. B., Zhang, R., Zhang, J., Giangrande, S. E., and Wang, J.: Deep Convection-Driven Downward Transport of Trace Gases and Aerosols From the Free Troposphere to the Boundary Layer, Geophysical Research Letters, 53, e2025GL119490, https://doi.org/10.1029/2025GL119490, 2026.

Neese, F.: The ORCA program system, WIREs Comput. Mol. Sci., 2, 73–78, https://doi.org/10.1002/wcms.81, 2012.

Ning, A., Liu, L., Zhang, S., Yu, F., Du, L., Ge, M., and Zhang, X.: The critical role of dimethylamine in the rapid formation of iodic acid particles in marine areas, npj Clim Atmos Sci, 5, 92, https://doi.org/10.1038/s41612-022-00316-9, 2022.

Ning, A., Shen, J., Zhao, B., Wang, S., Cai, R., Jiang, J., Yan, C., Fu, X., Zhang, Y., Li, J., Ouyang, D., Sun, Y., Saiz-Lopez, A., Francisco, J. S., and Zhang, X.: Overlooked significance of iodic acid in new particle formation in the continental atmosphere, Proc. Natl. Acad. Sci. U.S.A., 121, e2404595121, https://doi.org/10.1073/pnas.2404595121, 2024.

Peterson, K. A., Figgen, D., Goll, E., Stoll, H., and Dolg, M.: Systematically convergent basis sets with relativistic pseudopotentials. II. Small-core pseudopotentials and correlation consistent basis sets for the post-d group 16–18 elements, J. Chem. Phys., 119, 11113–11123, https://doi.org/10.1063/1.1622924, 2003.

Pope, C. A. and Dockery, D. W.: Health Effects of Fine Particulate Air Pollution: Lines that Connect, J. Air Waste Manage. Assoc., 56, 709–742, https://doi.org/10.1080/10473289.2006.10464485, 2006.

Qi, X., Li, Z., Zhao, C., Zhang, Q., and Zhou, Y.: Environmental impacts of Arctic shipping activities: A review, Ocean Coast. Manag., 247, 106936, https://doi.org/10.1016/j.ocecoaman.2023.106936, 2024.

Randel, W. J., Park, M., Emmons, L., Kinnison, D., Bernath, P., Walker, K. A., Boone, C., and Pumphrey, H.: Asian Monsoon Transport of Pollution to the Stratosphere, Science, 328, 611–613, https://doi.org/10.1126/science.1182274, 2010.

Ranjithkumar, A., Gordon, H., Williamson, C., Rollins, A., Pringle, K., Kupc, A., Abraham, N. L., Brock, C., and Carslaw, K.: Constraints on global aerosol number concentration, $SO_2$ and condensation sink in UKESM1 using ATom measurements, Atmos. Chem. Phys., 21, 4979–5014, https://doi.org/10.5194/acp-21-4979-2021, 2021.

Salignat, R., Rissanen, M., Iyer, S., Baray, J.-L., Tulet, P., Metzger, J.-M., Brioude, J., Sellegri, K., and Rose, C.: Measurement report: Insights into the chemical composition and origin of molecular clusters and potential precursor molecules present in

https://doi.org/10.5194/egusphere-2026-1771
Preprint. Discussion started: 20 April 2026


the free troposphere over the southern Indian Ocean: observations from the Maïdo Observatory (2150 m a.s.l., Réunion), Atmos. Chem. Phys., 24, 3785–3812, https://doi.org/10.5194/acp-24-3785-2024, 2024.

Sarr, S., Graton, J., Rahali, S., Montavon, G., and Galland, N.: Delocalized relativistic effects, from the viewpoint of halogen bonding, Phys. Chem. Chem. Phys., 23, 4064–4074, https://doi.org/10.1039/D0CP05840H, 2021.

Schmitz, G. and Elm, J.: Assessment of the DLPNO Binding Energies of Strongly Noncovalent Bonded Atmospheric Molecular Clusters, ACS Omega, 5, 7601–7612, https://doi.org/10.1021/acsomega.0c00436, 2020.

Shen, J., Russell, D. M., DeVivo, J., Kunkler, F., Baalbaki, R., Mentler, B., Scholz, W., Yu, W., Caudillo-Plath, L., Sommer, E., Ahongshangbam, E., Alfaouri, D., Almeida, J., Amorim, A., Beck, L. J., Beckmann, H., Berntheusel, M., Bhattacharyya, N., Canagaratna, M. R., Chassaing, A., Cruz-Simbron, R., Dada, L., Duplissy, J., Gordon, H., Granzin, M., Große Schute, L., Heinritzi, M., Iyer, S., Klebach, H., Krüger, T., Kürten, A., Lampimäki, M., Liu, L., Lopez, B., Martinez, M., Morawiec, A., Onnela, A., Peltola, M., Rato, P., Reza, M., Richter, S., Rörup, B., Sebastian, M. K., Simon, M., Surdu, M., Tamme, K., Thakur, R. C., Tomé, A., Tong, Y., Top, J., Umo, N. S., Unfer, G., Vettikkat, L., Weissbacher, J., Xenofontos, C., Yang, B., Zauner-Wieczorek, M., Zhang, J., Zheng, Z., Baltensperger, U., Christoudias, T., Flagan, R. C., El Haddad, I., Junninen, H., Möhler, O., Riipinen, I., Rohner, U., Schobesberger, S., Volkamer, R., Winkler, P. M., Hansel, A., Lehtipalo, K., Donahue, N. M., Lelieveld, J., Harder, H., Kulmala, M., Worsnop, D. R., Kirkby, J., Curtius, J., and He, X.-C.: New particle formation from isoprene under upper-tropospheric conditions, Nature, 636, 115–123, https://doi.org/10.1038/s41586-024-08196-0, 2024.

Sipilä, M., Sarnela, N., Jokinen, T., Henschel, H., Junninen, H., Kontkanen, J., Richters, S., Kangasluoma, J., Franchin, A., Peräkylä, O., Rissanen, M. P., Ehn, M., Vehkamäki, H., Kurten, T., Berndt, T., Petäjä, T., Worsnop, D., Ceburnis, D., Kerminen, V.-M., Kulmala, M., and O'Dowd, C.: Molecular-scale evidence of aerosol particle formation via sequential addition of $HIO_3$, Nature, 537, 532–534, https://doi.org/10.1038/nature19314, 2016.

Tost, H.: Chemistry–climate interactions of aerosol nitrate from lightning, Atmos. Chem. Phys., 17, 1125–1142, https://doi.org/10.5194/acp-17-1125-2017, 2017.

Twohy, C. H., Clement, C. F., Gandrud, B. W., Weinheimer, A. J., Campos, T. L., Baumgardner, D., Brune, W. H., Faloona, I., Sachse, G. W., Vay, S. A., and Tan, D.: Deep convection as a source of new particles in the midlatitude upper troposphere, J. Geophys. Res., 107, https://doi.org/10.1029/2001JD000323, 2002.

Wang, J., Krejci, R., Giangrande, S., Kuang, C., Barbosa, H. M. J., Brito, J., Carbone, S., Chi, X., Comstock, J., Ditas, F., Lavric, J., Manninen, H. E., Mei, F., Moran-Zuloaga, D., Pöhlker, C., Pöhlker, M. L., Saturno, J., Schmid, B., Souza, R. A. F., Springston, S. R., Tomlinson, J. M., Toto, T., Walter, D., Wimmer, D., Smith, J. N., Kulmala, M., Machado, L. A. T., Artaxo, P., Andreae, M. O., Petäjä, T., and Martin, S. T.: Amazon boundary layer aerosol concentration sustained by vertical transport during rainfall, Nature, 539, 416–419, https://doi.org/10.1038/nature19819, 2016.

Wang, M., Xiao, M., Bertozzi, B., Marie, G., Rörup, B., Schulze, B., Bardakov, R., He, X.-C., Shen, J., Scholz, W., Marten, R., Dada, L., Baalbaki, R., Lopez, B., Lamkaddam, H., Manninen, H. E., Amorim, A., Ataei, F., Bogert, P., Brasseur, Z., Caudillo, L., De Menezes, L.-P., Duplissy, J., Ekman, A. M. L., Finkenzeller, H., Carracedo, L. G., Granzin, M., Guida, R., Heinritzi, M., Hofbauer, V., Höhler, K., Korhonen, K., Krechmer, J. E., Kürten, A., Lehtipalo, K., Mahfouz, N. G. A.,

https://doi.org/10.5194/egusphere-2026-1771
Preprint. Discussion started: 20 April 2026


Makhmutov, V., Massabò, D., Mathot, S., Mauldin, R. L., Mentler, B., Müller, T., Onnela, A., Petäjä, T., Philippov, M., Piedehierro, A. A., Pozzer, A., Ranjithkumar, A., Schervish, M., Schobesberger, S., Simon, M., Stozhkov, Y., Tomé, A., Umo, N. S., Vogel, F., Wagner, R., Wang, D. S., Weber, S. K., Welti, A., Wu, Y., Zauner-Wieczorek, M., Sipilä, M., Winkler, P. M., Hansel, A., Baltensperger, U., Kulmala, M., Flagan, R. C., Curtius, J., Riipinen, I., Gordon, H., Lelieveld, J., El-Haddad, I., Volkamer, R., Worsnop, D. R., Christoudias, T., Kirkby, J., Möhler, O., and Donahue, N. M.: Synergistic $HNO_3$–$H_2SO_4$–$NH_3$ upper tropospheric particle formation, Nature, 605, 483–489, https://doi.org/10.1038/s41586-022-04605-4, 2022.

Wang, Y., Fu, X., Wu, D., Wang, M., Lu, K., Mu, Y., Liu, Z., Zhang, Y., and Wang, T.: Agricultural Fertilization Aggravates Air Pollution by Stimulating Soil Nitrous Acid Emissions at High Soil Moisture, Environ. Sci. Technol., 55, 14556–14566, https://doi.org/10.1021/acs.est.1c04134, 2021.

Williamson, C. J., Kupc, A., Axisa, D., Bilsback, K. R., Bui, T., Campuzano-Jost, P., Dollner, M., Froyd, K. D., Hodshire, A. L., Jimenez, J. L., Kodros, J. K., Luo, G., Murphy, D. M., Nault, B. A., Ray, E. A., Weinzierl, B., Wilson, J. C., Yu, F., Yu, P., Pierce, J. R., and Brock, C. A.: A large source of cloud condensation nuclei from new particle formation in the tropics, Nature, 574, 399–403, https://doi.org/10.1038/s41586-019-1638-9, 2019.

Xiao, Q., Zhang, J., Wang, Y., Ziemba, L. D., Crosbie, E., Winstead, E. L., Robinson, C. E., DiGangi, J. P., Diskin, G. S., Reid, J. S., Schmidt, K. S., Sorooshian, A., Hilario, M. R. A., Woods, S., Lawson, P., Stamnes, S. A., and Wang, J.: New particle formation in the tropical free troposphere during CAMP$^2$ Ex: statistics and impact of emission sources, convective activity, and synoptic conditions, Atmos. Chem. Phys., 23, 9853–9871, https://doi.org/10.5194/acp-23-9853-2023, 2023.

Xu, W., Liu, L., Cheng, M., Zhao, Y., Zhang, L., Pan, Y., Zhang, X., Gu, B., Li, Y., Zhang, X., Shen, J., Lu, L., Luo, X., Zhao, Y., Feng, Z., Collett Jr., J. L., Zhang, F., and Liu, X.: Spatial–temporal patterns of inorganic nitrogen air concentrations and deposition in eastern China, Atmos. Chem. Phys., 18, 10931–10954, https://doi.org/10.5194/acp-18-10931-2018, 2018.

Yu, H., Ren, L., Huang, X., Xie, M., He, J., and Xiao, H.: Iodine speciation and size distribution in ambient aerosols at a coastal new particle formation hotspot in China, Atmos. Chem. Phys., 19, 4025–4039, https://doi.org/10.5194/acp-19-4025-2019, 2019.

Zhang, R.: Getting to the Critical Nucleus of Aerosol Formation, Science, 328, 1366–1367, https://doi.org/10.1126/science.1189732, 2010.

Zhang, R., Khalizov, A., Wang, L., Hu, M., and Xu, W.: Nucleation and Growth of Nanoparticles in the Atmosphere, Chem. Rev., 112, 1957–2011, https://doi.org/10.1021/cr2001756, 2012.

Zu, H., Zhang, S., Liu, L., and Zhang, X.: The vital role of sulfuric acid in iodine oxoacids nucleation: impacts of urban pollutants on marine atmosphere, Environ. Res. Lett., https://doi.org/10.1088/1748-9326/ad193f, 2023.

Zu, H., Chu, B., Lu, Y., Liu, L., and Zhang, X.: Rapid iodine oxoacid nucleation enhanced by dimethylamine in broad marine regions, Atmos. Chem. Phys., 24, 5823–5835, https://doi.org/10.5194/acp-24-5823-2024, 2024.